Nano Energy 59 (2019) 422–433

Contents lists available at ScienceDirect

Nano Energy

journal homepage: www.elsevier.com/locate/nanoen

Full paper

A Universal high accuracy wearable pulse monitoring system via high sensitivity and large linearity graphene pressure sensor

Jiang He[a,c], Peng Xiao[a], Wei Lu[a,*], Jiangwei Shi[a], Ling Zhang[a,c], Yun Liang[a,c], Caofeng Pan[b,c,**], Shiao-Wei Kuo[d], Tao Chen[a,c,**]

[a] Key Laboratory of Marine Materials and Related Technologies, Zhejiang Key Laboratory of Marine Materials and Protective Technologies, Ningbo Institute of Materials Technology and Engineering, Chinese Academy of Sciences, Ningbo 315201, PR China
[b] Beijing Key Laboratory of Micro-nano Energy and Sensor, Beijing Institute of Nanoenergy and Nanosystems, Chinese Academy of Sciences, Beijing 100083, PR China
[c] University of Chinese Academy of Sciences, Beijing 100049, PR China
[d] Department of Material and Optoelectronic Science, Center of Crystal Research, National Sun Yat-Sen University, 804, Kaohsiung, Taiwan

ARTICLE INFO

Keywords:
Graphene
Self-assembly
Piezo-resistive sensor
Wearable devices
Pulse monitoring

ABSTRACT

Long-term accurate pulse monitoring can provide much physiological parameter information in a non-invasive way. A versatile pressure sensor with high sensitivity over a wide linear range (up to 10 kPa) is thus especially desired for this purpose. However, the trade-off between linearity region and sensitivity has not been well balanced. Despite micro/nanostructure morphologies, our simulation and mechanism analyses found that a thinner structure and better conductivity property of the sensing layer contribute to a larger linearity range and higher sensitivity, respectively. However, these two properties are often difficult to achieve simultaneously in one traditional material. Herein, a novel material design strategy is developed to fabricate a self-assembled graphene sensing film, in which the conductivity and thickness can be well balanced. As a result, our sensor exhibits unprecedented comprehensive properties with both high sensitivity (1875.53 kPa^{-1}) and wide linear detection range (0–40 kPa). The sensor is also endowed with good stability and high peak signal-noise ratio (78 dB). Taking advantages of these performances, a universal high accuracy wireless and wearable pulse monitoring system was built. This platform first provides the subtle arterial pulse signal information even under the interference of strong body movement in real-time (during running or cycling), which could not have been realized before. This wearable system is expected to provide more rich and accurate information for personalized diagnostic applications in the future.

1. Introduction

Long-term pulse monitoring during daily life can provide important information about the arterial physical situation for non-invasive medical diagnosis. Nowadays , photoplethysmography (PPG) is the most widely commercially applied technologies for smartwatch pulse measurement, such as apple watch. However, these devices are vulnerable to ambient light variation and body movement. Thus, it is difficult to precisely measure the subtle signals, which are vital to diagnosis, in our pulse wave during our daily life. Therefore, developing a pulse sensor which can acquire accurate pulse signal even under the interference of light variation and body movement is urgent and significantly important. Recently, various new concepts about soft wearable health monitoring devices are attracting increasing attention in modern electronics, because they can continuously record such physiological information of an individual from human skin. Over the past years, significant advances have been achieved in noninvasive health-monitoring devices by employing pressure-sensitive electronic skin [1–13]. Among them, piezo-resistive devices, which can transduce applied pressure into the electrical signal, are extensively used in physical data collection (such as pulsation) because of simple structure, low operating voltages, and ease of signal processing [11,12]. However, as a most arterial trees are deep under the skin, most of the pulse signal is fade-out during its long transmitting process in soft tissue, thus resulting in extremely low pulse signal or even disappearing on our skin surface. Additionally, the strong noise signal caused by body movement or ambient variation may overwhelm the vulnerable arterial pulse signal, which makes the precisely real-time measurement of pulse wave

* Corresponding author.
** Correspondence to: Ningbo Institute of Materials Technology and Engineering, Chinese Academy of Sciences, Ningbo 315201, PR China.
E-mail addresses: luwei@nimte.ac.cn (W. Lu), cfpan@binn.cas.cn (C. Pan), tao.chen@nimte.ac.cn (T. Chen).

https://doi.org/10.1016/j.nanoen.2019.02.036
Received 30 January 2019; Accepted 14 February 2019
Available online 15 February 2019

even more difficult in daily life [14]. It can be a promising candidate to overcome such problem by employing an external force to make the sensor closer to arterial to improve the signal-to-noise ratio. However, although high sensitivity of applied gentle touch (pressure up to ≈10 kPa) is generally needed for pressure-sensitive electronic skin applications, most of these reported sensors are not able to maintain high sensitivity at such upper pressure value [8,9,11,15]. Furthermore, since most of these reported sensors don't have a wide linear detection range, it becomes very difficult for the users to obtain accurate information from the sensor output in daily life. Therefore, it is of great urgency and importance to developing new pressure-sensitive sensors with both high sensitivity and wide linearly sensitive regime (> 10 kPa).

Normally, the elastic 3D microstructures and conductive sensing layer are two key elements in pressure sensors. In order to achieve high sensitivity in a wide linear range, great efforts have been devoted to the improvement of the performance by the development of novel elastic microstructure geometries (such as pyramids [15,16], hemispheres [17], prisms [12], epidermis microstructure [18]) on the sensor. However, few study attentions have been paid to optimize the structure and electrical properties of the sensing layer on microstructure elastomer. An ideal sensing layer should have highly conductive, mechanically strong and ultrathin structure, which can easily be self-attached to the sensor surface without covering its elaborate 3D microstructures. Nevertheless, the mechanical and electrical properties are normally determined by the thickness of film materials. For instance, when one tries to improve the mechanical strength and conductivity of the film, the overall thickness also increases considerably and the subtle 3D microstructures are thus covered. Single-atom-thick graphene, the stiffest, thinnest and strongest material, is widely known as an excellent heat/electricity conductor [19–21], and can thus be an ideal candidate to be used as such conduct layer. However, the fabrication process of highly conducting CVD graphene film is often complicated, involving costly equipment due to ultravacuum and high temperature conditions in technology. Chemical approaches to large-scale produce highly conducting graphene film remain elusive, as the harsh processes often create defects in the crystallographic structure of graphene, leading to poor electronic performance [22–26]. Besides, the delicate processes to transfer nanoscale thick graphene film too soft elaborate 3D microstructures elastomer without structural damage is another great challenge [21,27].

Herein, we report a mass producible and all-solution processable, yet simple and environmentally friendly strategy for high-performance piezo-resistive pressure sensor based on highly conductive interfacially self-assembled graphene (ISG) film (Fig. 1). An ultra-large macroscopic ISG film is spontaneously assembled by graphene nanoplatelets sprayed on liquid/air surface via the assistance of capillary force induced compression (Fig. 1a-b). The as-prepared ISG film can be easily transferred to micropatterned PDMS elastomer and self-attached to the elaborate 3D microstructures on sensor surface after annealing treatment (Fig. 1c). The sensitivity and linearity region has been well balanced by regulating the structure of the ISG film. Based on simulation and mechanism analysis, the high conductivity property and nanoscale thickness of ISG film contribute to the excellent sensitivity and wide linear detection range, respectively. Additionally, the pressure sensor is proved to exhibit high durability of 15,000 cycles, fast response (0.5 ms) and recover (0.8 ms) time and a low limit of detection of 1.8 Pa. These promising advantages of the wearable sensor allow us to record the very weak and subtle arterial pulse signal information that has not been realized before, which enables us to obtain accurate pulse signal along the arterial on arm from the sensor output signal (Fig. 1**d**). Furthermore, the powerful sensor can even provide us very clear real-time pulse signal during daily life and excise process (Fig. 1**e**). Regarding the facile synthesis of our sensory materials and their robust sensing ability, the proposed sensor could potentially be constructed as next-generation wearable intelligent mobile diagnosis, and prevention of cardiovascular disease in the future smart physiological real-time monitoring device.

2. Materials and methods

2.1. Preparation of large-area ISG

Few-layer graphene sheets are exfoliated from graphite through the

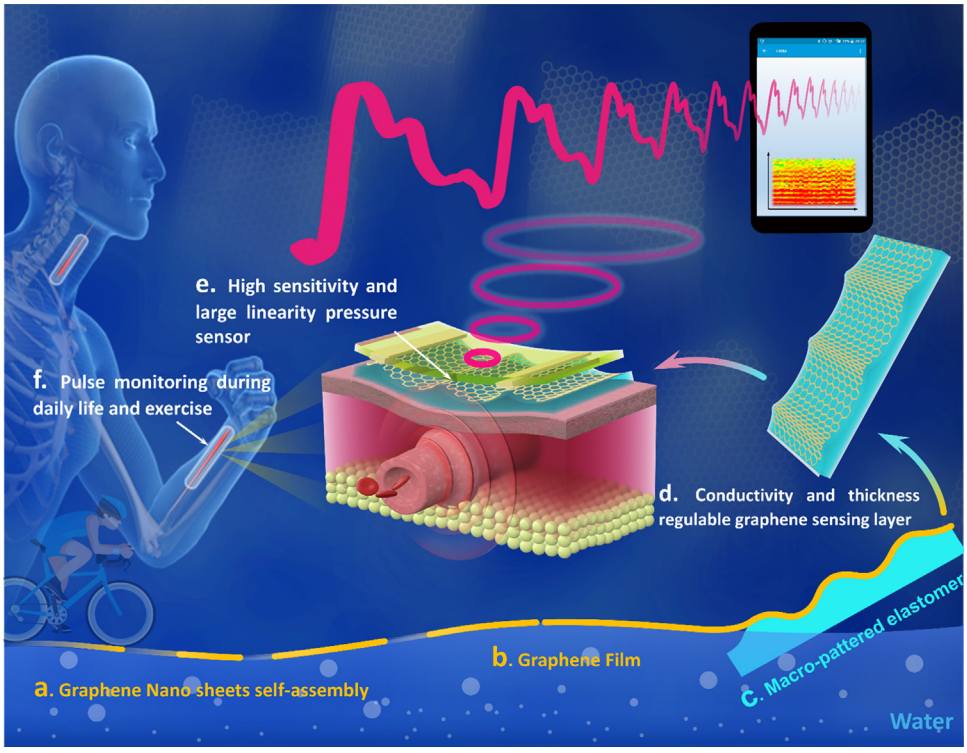

Fig. 1. Large-area and highly conductive self-assembled graphene film (a-b) can be formed on the water-air interface via spraying. (c) The unique film can be easily transferred and assembled into ultrathin conductive sensing layer on micropatterned (d) elastomer surfaces to form a pressure-sensitive electronic skin piezoresistive sensor. (e) The high-performance sensor exhibits both high sensitivity and wide linear range, thus making the device being capable of detecting the weak signal and recording pulse signal accurately in a real-time during daily life and exercise (f).

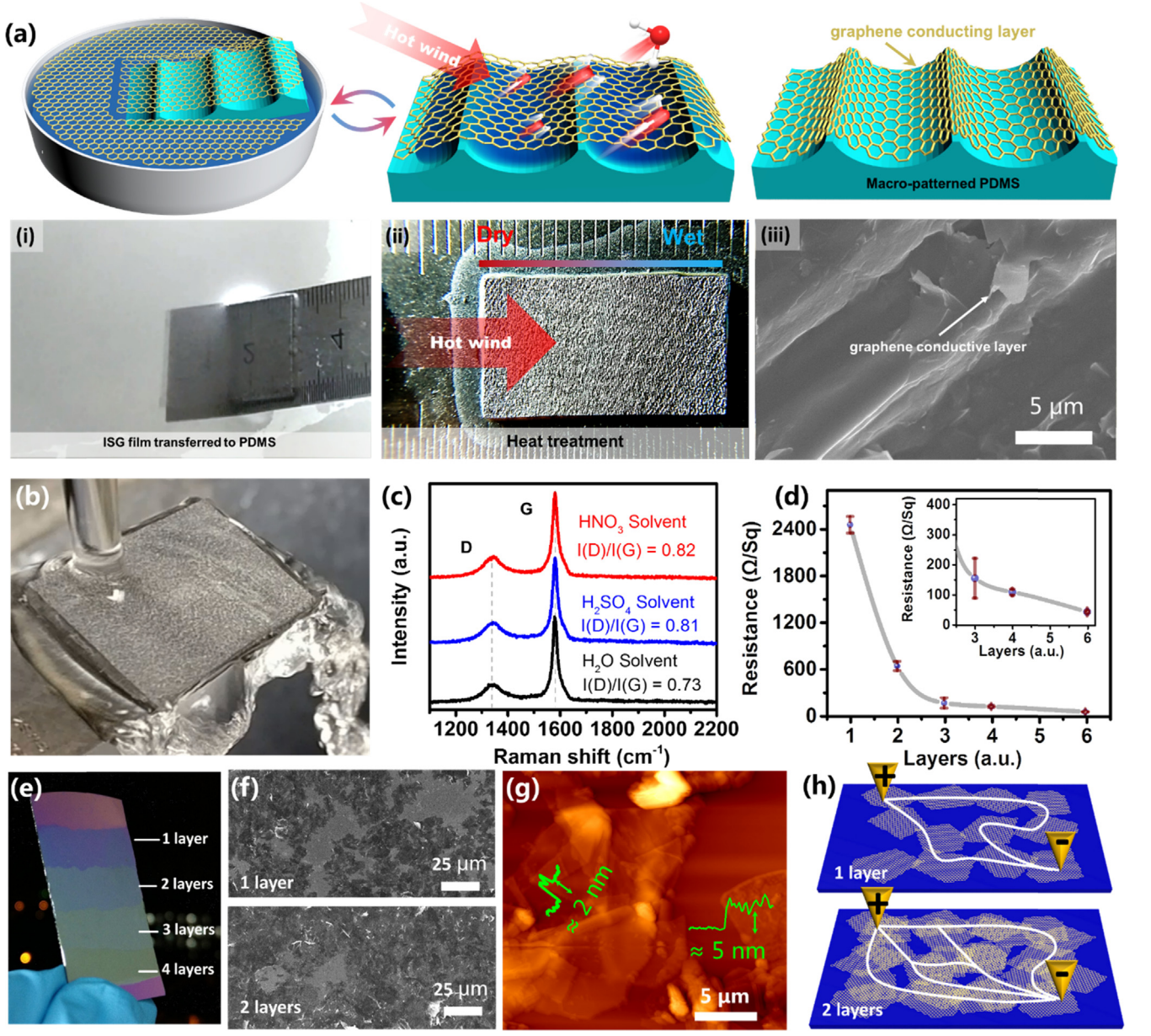

Fig. 2. Fabrication of PDMS-Gr. (a) Schematic of the fabrication process of PDMS-Gr: (i) ISG film transferred to macro-pattered PDMS. (ii) Heat treatment process. (iii) SEM images of macro-pattered PDMS-Gr elastomer. (b) Photographs of PDMS-Gr under water flow. (c) Raman spectra of PDMS-Gr samples recorded after being treated by different chemicals (HNO_3, H_2SO_4, H_2O) for 15 days. Photograph (e), SEM (f) and AFM (g) images of ISG film transferred and laminated on a silicon wafer. (h) Conductivity mechanism of ISG films in respect to different laminations.

mechanical exfoliation method [24]. The lateral size of the exfoliated graphene is about 2–20 μm and the thickness is 2 ~ 7 nm. The graphene sheets were rinsed thoroughly with anhydrous ethanol and dried in a stream of nitrogen before use. Ethanol and deionized water are used as rinsing solvents. The graphene sheets were first dispersed in anhydrous ethanol solution (0.5 mg/ml), followed by strong ultrasonication for 2 h to form a stable dispersion with appropriate aging time. Then, the ethanol-assisted graphene dispersion solution (≈ 200 ml/m^2) was sprayed onto the water surface, resulting in the formation of uniform Langmuir monolayers at the liquid/air interface. Subsequently, micro-porous sponges were selected to put on one side of the interface to quickly siphon water from the system. The homogeneous Langmuir monolayers were then closely packed toward the opposite direction of the siphone direction. (video 1) When the movement of the film stopped and further siphoning could not drive the film, the film with was a closely packed structure was ultimately prepared.

Supplementary material related to this article can be found online at doi:10.1016/j.nanoen.2019.02.036.

2.2. Fabrication of the pressure sensors

The silk molded micro-patterned PDMS film was first prepared according to the reported method [12]. The as-prepared ISG films were then transferred onto the patterned surface of PDMS film. In the transferring process, the micro-patterned PDMS films were attached to plates (a ruler) and gradually inserted into the aqueous solution (45 degrees to the water surface). The plates were then lifted gradually to pick up ISG ultrathin films and to attach them over the PDMS films. Finally, the PDMS-Gr films were annealed by hot wind (≈200 °C) for 10 min to improve their stability and assembled onto interdigitated Ni/Au electrode (IDE) as a pressure sensor. The as-prepared sensor was connected to data acquisition and computer to collect data.

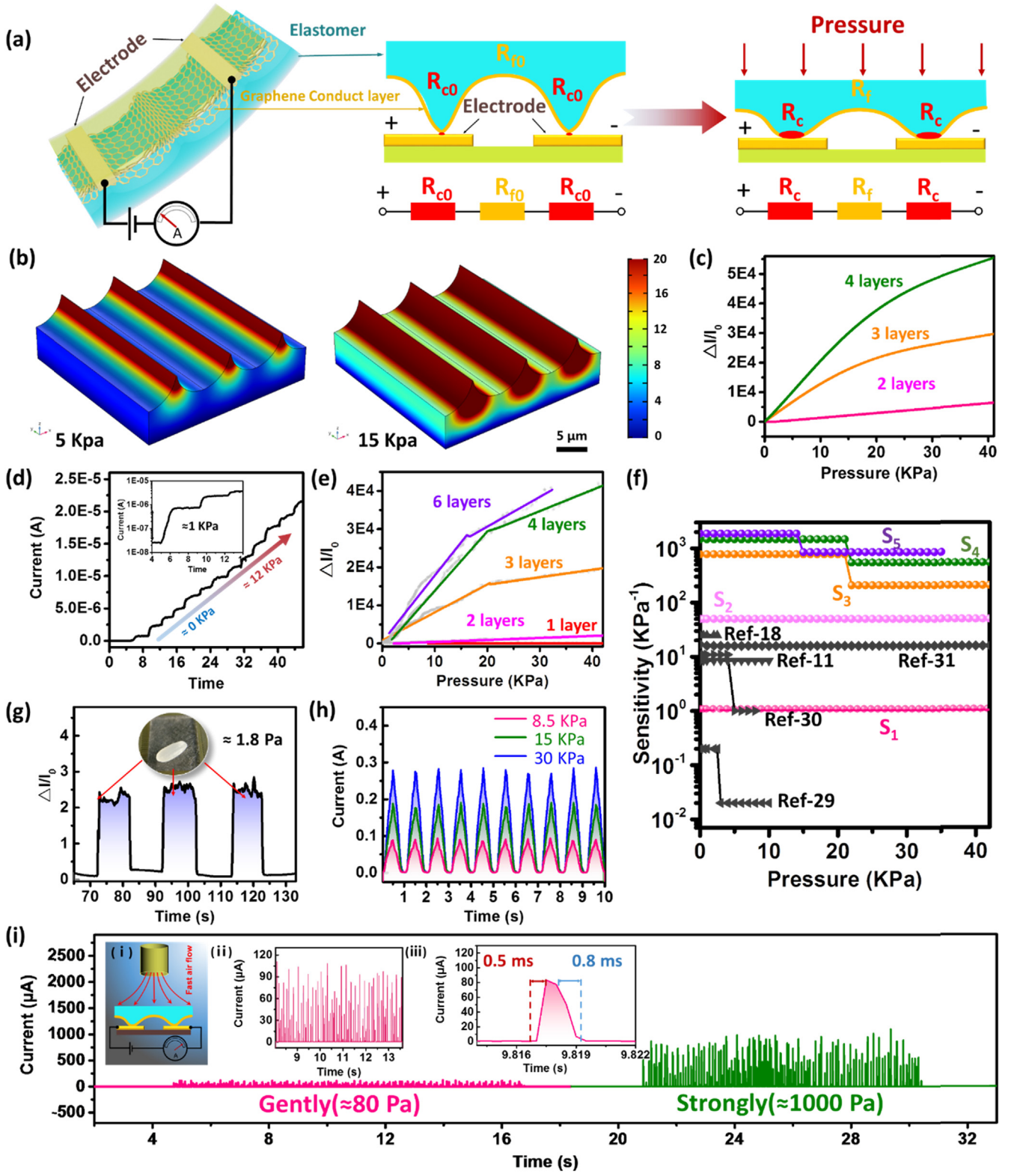

Fig. 3. Fabrication of pressure sensor and quantitative study of its performance. (a) Schematic illustration of the fabrication and operating principle of the pressure sensor. Under normal compressive pressure, the increase of contacting area between PDMS-Gr and electrode contributes to the linear sensitivity over a wide pressure range. (b) The displacement distribution of the simulation results for the macro-pattered elastomer at different external loading pressure. (c) The simulation results of resistance variation versus applied pressure for macro-pattered elastomer with different ISG film layers. (d) The current output of pressure sensors constructed with S_2. (e) Pressure-response sensitivities curves for pressure sensors constructed with different layer ISG films. (f) Performance comparison with the previously reported piezo-resistive sensor. (g) The S_4 can detect the application of very tiny pressures. It shows the real-time current change after placing and removing a rice (≈20 mg), corresponding to a pressure of only 1.8 Pa. (h) Real-time I-t curves of the S_4 pressure sensor device responding to three large repeated applied pressure. (i) The sensor (S_2) can respond to fast air flow with two different strength. Inset Figures (iii) suggests its ultrafast response and recovery times.

2.3. Characterization

Electrical sheet resistance of ISG films on the quartz plates (1 × 1 cm) was measured with the 4-point probe (Materials of Development Corporation model CMTSR2000N). Three samples were prepared for each film, and each sample was tested by the 4-point probe three times. Atomic force microscopy (AFM) images were taken by a multimode AFM (Being Nano-Instruments, Ltd) operating in tapping mode using silicon cantilevers (spring constant: 0.15 Nm^{-1}, resonant frequency: 12 kHz for cantilever of contact mode, spring constant: 3–40 Nm^{-1}, resonant frequency: 75–300 kHz for cantilever of tapping mode). Hitachi-S4800 field-emission scanning electron microscope (FE-SEM) was used to investigate the morphology of graphene on the silicon substrate. The Raman scattering measurements were performed at room temperature on a Raman system (in Via-reflex, Renishaw) with confocal microscopy. The solid-state diode laser (532 nm) was used as an excitation source with a frequency range of 3200–1000 cm^{-1}. The response time was determined using an Oscilloscope OWON HDS1021MN. The electrical impendence measurements were carried out using an electrochemical workstation CHI660E. The electrochemical workstation (CH Instruments 660D) was used to measure I-t curves in real-time, and the Source-Drain voltage was 1 VDC. The loading of applied force was carried out with a testing machine (NSTRON CORPORATION 5542).

3. Results and discussion

Our strategy for fabricating interracially self-assembled graphene film is schematically illustrated in Fig. S1. Once the mechanically exfoliated graphene nanosheets dispersion in ethanol is sprayed onto the surface of the water, they will spontaneously and rapidly form a layer of large area graphene Langmuir thin film (Fig. S1-a). After using a porous sponge to siphon one side of the water surface, the graphene nanosheets will self-assemble into closely packed state driven by capillary force [28] (Fig. S1-b, Fig. S1-c, and **Video-1**). As a result, an ultra-large-area graphene film is obtained (Fig. 2**a-ii**), which could be easily transferred to glass (Fig. S2) or a silicon wafer surface (Fig. 2**e**).

The overall fabrication procedure of macro-pattered PDMS elastomer with self-attached conductive graphene film (PDMS-Gr) is illustrated in Fig. 2. A silk-molded flexible micropatterned PDMS thin film was first fabricated according to the previously reported method [12], which was then used to transfer the as-prepared ISG film (Fig. 2**a-i**). After hot treatment, the water molecules will evaporate from the gap between the ISG film and PDMS substrate, making the graphene sheets self-attached to the 3D microtopography structure on PDMS surface strongly (Fig. 2**a-ii** and Fig. S3). Repeating this transferring-hot-treating process (1–6 times) will result in the formation of 3D microtopography guided graphene conducting film with tunable conductivity on the macro-pattered PDMS elastomer. The SEM images (Fig. 2**a-iii**) indicate that the graphene nanosheets are tightly fitted to the patterned PDMS surface after thermal treatment, suggesting the great possibility of the sensing elements to work stably during long-term cycles. Further physical and chemical stability tests demonstrate that the ISG film can keep stable under water flow impact pressure (Fig. 2**b**). To test its chemical stability, we analyzed the chemical structure change of single-layer ISG films treated by different solvents (DI water, 0.1 mol L^{-1} sulfuric acid, or 0.1 mol L^{-1} nitric acid, treated for 24 h). As seen in Fig. 2**c**, the Raman spectroscopy showed a very small I_D/I_G (= 0.73) ratio (the intensity ratio of D band and G band) of ISG film. As the G and D bands are associated with the graphite-like structures and graphene edge (or a graphene piece that contains defects), respectively, therefore, the small I_D/I_G ratio implies the high quality of graphene film. By contrast, the I_D/I_G values of sulfuric acid (I_D/I_G = 0.81) solvent and nitric acid (I_D/I_G = 0.82) treated samples (Three samples were immersed in 40°Cdeionized water, 1 M sulfuric acid solvent and 1 M nitric acid solvent, respectively, for 15 days) show little change compared to original sample, indicating the good chemical stability of ISG films. For the purpose of modulating their conductive and sensory properties, the films with different ISG layers were prepared. The transferred graphene films present quite good conductivity. The quantitative research shows that the average sheet resistance of ISG film gradually decreases from 2453 ± 107 Ω sq^{-1} to 42 ± 3 Ω sq^{-1} as the layer increases from one to six (Fig. 2**d**). Interesting, when the layer is less than three, the resistance falls dramatically with an increase in layer number, which was primarily attributed to the decrease of the gaps between each nano thick graphene sheets (Fig. 2**e-h**). While there are only a few gaps on ISG film surface for films with more than 3 layers (Fig. S4), a good linear relationship is observed between the sheet resistance and film thickness (Fig. 2**d**).

The structure of our soft pressure sensor is illustrated in Fig. 3**a**. Briefly, the sensor is constructed by placing one macro-pattered PDMS-Gr soft film onto flexible Ni/Au interdigital electrode (IDE) face-to-face (Fig. 3**a-left**). The resistance of the device is the average value of every contact resistance of sensitive sites between top PDMS-Gr and bottom IDE. Under low pressure, the small contact area (A_c) leading to a large contact resistance (Fig. 3**a-middle**). When pressure is applied, the conductance of the sensor dramatically increases due to increasing contacting sites of PDMS-Gr and IDE (Fig. 3**a-right**). To understand the current changes during the loading process, a circuit model has been proposed to calculate the resistance contribution. The total current can be obtained using the following equation:

$$I = U/(R_s + R_c)$$

where U, R_s, and R_c are the operating voltage, the resistance of PDMS-Gr and resistance of contact interfaces, respectively. The R_s is a constant value which can be regulated by the deposited graphene layers. The R_c mainly contributes to the total resistance change because of the rapidly increased contact interface under loading pressure. Generally, the R_c decreases as a result of the dramatically increased contact area caused by a small pressure (P). In order to quantitatively describe the sensing performance for our sensor, the MATLAB model of the current (I) change under loading pressure (P) is established. According to the experiments, the simplified PDMS-Gr 3D model with a defined height distribution matrix is built. After that, the element of the contact area is simulated under different degrees of compression (Fig. 3**b** and Fig. S5). Each element is regarded as a small resistance, and the total resistance could be regarded as these resistances with a parallel connection. Then the relation between structure compressing degree and resistance of PDMS-Gr can be achieved. By inverting the relation between compressing degree and pressure recorded in the experiments, the relation of current and pressure of the sensor is summarized in Fig. 3**c**. The sensor model exhibits a high and regulable sensitivity and a broad linearity range. On one side, the sharp microstructures on elastomer reduce the initial contact area, which favors high sensitivity [12]. On the other hand, the nanoscale thin PDMS-Gr layer remains the subtle microstructures and deformation space on the elastomer, which ensure its high sensitivity in a large sensing region. Furthermore, the excellent conductivity property enables graphene film transforms and transfers the mechanical deformation signal to the current signal with high efficiency, which is critical to enhancing the sensitivity. To get insight into the relationships between sensitivity (S) and R_s, simulated mathematical relationships are provided as follows.

$$S = \frac{\partial\left(\frac{\triangle I}{I_0}\right)}{\partial P} = \frac{(R_s + R_{c0})K}{(PR_s + K)^2}$$

where S, P, and K are the sensitivity, applied pressure and a constant value determined by the microstructures on the elastomer, respectively. The simulated curve (Fig. 3**c**) and mathematical relationships both points out that a low resistance value of PDMS-Gr (R_s) is a key element for high sensitivity.

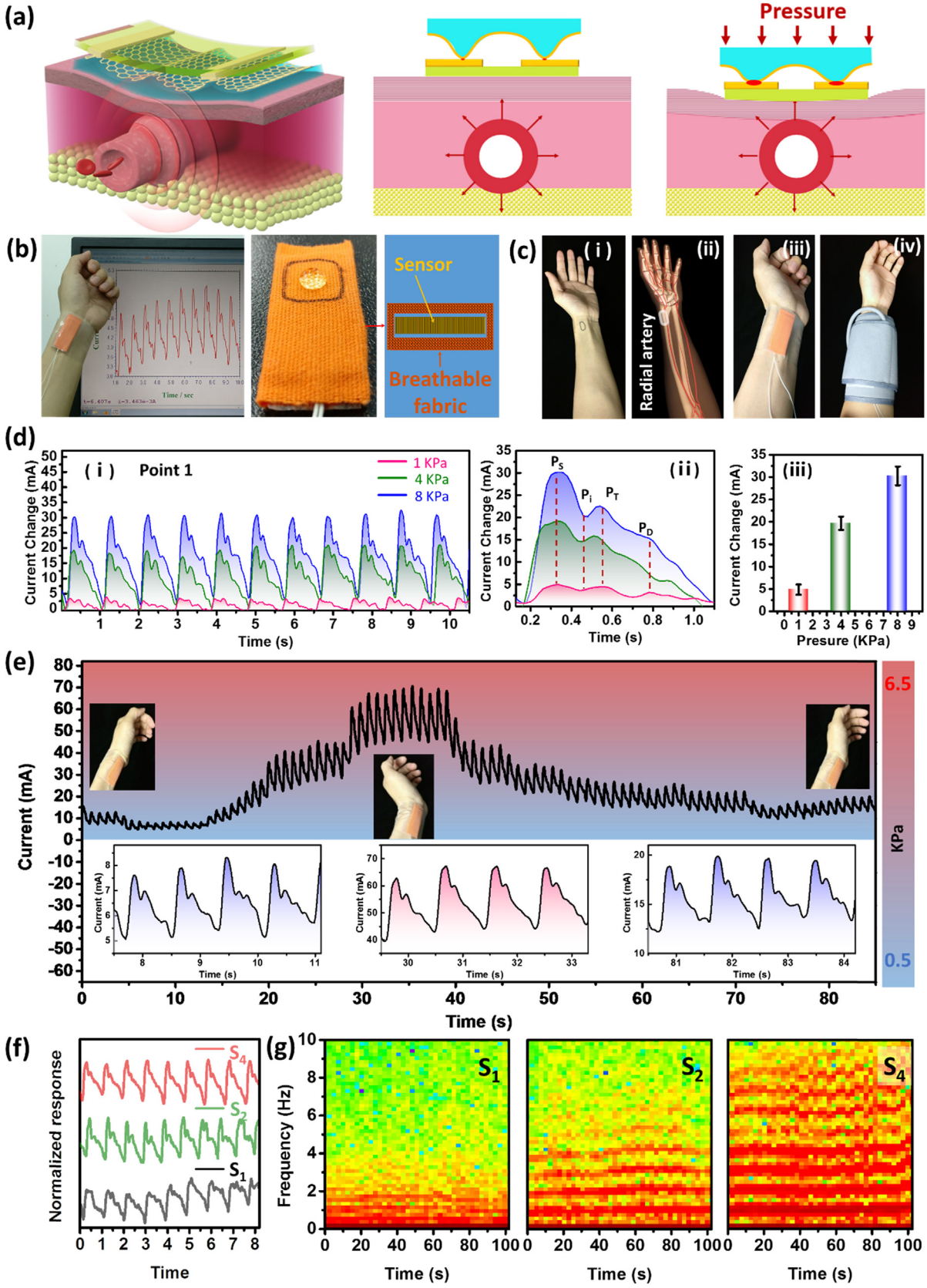

Fig. 4. Real-time high accuracy pulse wave monitoring under body motion interference. (a) Schematic illustration of artery pulse detection on the skin surface. The applied pressure forces the sensor close to the artery, which maximizes the signal from the artery pulse. (b) The artery pulse signal measured under different pressure. (c) Images of three identical contact points in artery pulse measurement project and the blood pressure cuff for accurate pre-charge pressure applied to the sensor. (d) The pulse signal measured under different applied pressure. (i and ii are extracted interpreted waveforms of the pulse; iii is the statistical data of the current change by applying variable pressure. The error bars represent the standard deviations.) (e) A real-time pulse signal (all the pulse signals are raw date without smooth) measured during wrist bending process. (f) The pulse signals of one volunteer and its corresponding frequency spectrums (g) measured by three sensors with different sensitivity.

The pressure sensing tests are conducted according to the previously reported method [12,15]. A thin glass plate of equal size with the area of 100 mm^2 (10 mm × 10 mm) was placed over the entire device to enlarge the lamination between the two flexible film sheets. The pressure from the PDMS-Gr and glass slide weight (≈1.14 g) is named as 'base pressure', while additional pressure is named as 'applied pressure'. As the applied pressure rises from 0 to 12 kPa, the conductance of sensor dramatically increased (from 10^{-8} A to 10^{-5} A) due to increasing contacting sites between top graphene film and the bottom electrode (Fig. 3**d**). It is found that the pressure sensor can respond in a very wide regime (From 0 kPa to 40 kPa) and the relative $\Delta I/I_0$ shows a quasi-linear dependence on the pressure (Fig. 3**e**). The slope of the curve can be defined as sensitivity ($S = \delta(\Delta I/I_0)/\delta p$, $\Delta I = I\text{-}I_0$, where p is the applied pressure, and I_0 and I are the resistance values without and with applied pressure, respectively) of the sensor. To study the effect of conductivity of ISG film on the sensing performance, the sensitivity of the pressure sensor devices (Sensor 1–5 (S_1- S_5),) based on different number of transferred ISG film layers (1 layer, 2 layer, 3 layer, 4 layer,6 layers, respectively) were compared. The experimental results coincident are with the theoretical simulation analysis well. Fig. 3**f** shows the current change ratio ($\Delta I/I_0$) relying on the applied normal pressure in regard to the layers of ISG film. It was found that most of the sensors (S_1, S_2, S_3, S_4) exhibit a large linear region from 0 kPa to 40 kPa. The sensitivity of the devices increases from 1.04 kPa^{-1} to 1875.5 kPa^{-1} as ISG film layers increases from 1 to 6. S_3, S_4 and S_5 show a quasi-bilinear dependence on the pressure. Take S_4 for example, at low pressure region (< 20 kPa), a well-behaved linear variation in the current change ratio with pressure gives an unprecedented pressure sensitivity of 1875.5 kPa^{-1}. At high pressure region (> 20 kPa), although a relative lower pressure sensitivity was experimentally observed, the S value is still high (S = 853.2 kPa^{-1}). Overall, as shown in Fig. 3**f**, S_2- S_5 exhibit much greater sensitivity over a wider linear range of applied pressure values than the previously reported pressure sensors [11,18,29–31]. It's worth to point that, as the gradual increasing thickness of PDMS-Gr, S_5 exhibit a dramatically narrow linear region comparing to other samples, which is due to the thick ISG film reduced the deformation space between the IDE and macrostructure. It can be concluded that the high conductivity property of ISG film mainly results in high sensitivity, while the nano-scale thickness of ISG film mainly results in the large linear range. It is noted that, due to the appropriate thickness and conductivity of ISG film on S_4, it shows the best overall performance sensitivity and wide linear range performance variation. Therefore, we mainly focus on S_4 devices in the following study.

The detection limit is another key parameter of the pressure sensor. Fig. 3**g** shows the transient response of the sensing device upon the loading and removal of small weight, such as a rice (≈20 mg), which shows the sensor has a very low detection limit (1.8 Pa) and good reproducibility. To further investigate the reproducibility of the sensor under high pressure, the conductance variation of the device was measured after repeatedly loading/unloading different applied pressure (8.5 kPa, 15 kPa, and 40 kPa) (Fig. 3**h**). Furthermore, the sensor shows also long-time stability during more than 15,000 loading/unloading cycles (Fig. S6), as well as a fast temporal response (2 ms) and recover time (3 ms) (Fig. S7). It's worth to point out that temporal response time may be limited by our instrument performance. In Fig. 3**i,** fast air flow was pumped to the surface of the sensor. Faster response and recovery speed could be observed.

Monitoring respiratory information (e.g. respiratory rate/depth) has become a simple yet powerful method for cardio-pulmonary function health status evaluation and disease diagnosis [10,13,32]. Respiratory monitoring using soft electronic material is particularly attractive because they are non-invasive and can simultaneously be adhered onto the skin surface for better comfort. For this purpose, a wireless wearable human breath real-time monitoring device is fabricated. The "smart belt" device consisting of a high performance pressure sensor could be worn around the waist. The signal of the sensor can be transduced and processed by microcontroller and uploaded to a computer or smartphone. The transceiver favors wireless data transmission to a Bluetooth-enabled smartphone for analysis or even sending the data to cloud servers (Fig. S8-a). Typically, one whole breathing cycle includes both inhalation and exhalation process. During the inhale process, the abdominal and chest cavity expand, which in turn increase the pressure on the sensor to generate an inhale signal. Reversely, when the individual exhales, the chest and abdominal cavity contract and thus decrease the pressure on the sensor to generate an opposite signal. Thus, the respiratory signals could be divided into a series of intervals of exhale and inhale time sequence: (T_1^{Ex}, T_1^{In}), (T_2^{Ex}, T_2^{In}), (T_3^{Ex}, T_3^{In})… (T_{n-1}^{Ex}, T_{n-1}^{In}), (T_n^{Ex}, T_n^{In}) (S8-b). Hence, each time interval (T_n^{Ex}, T_n^{In}) corresponding to one whole breathing cycle and the respiratory rate R_{res} in each breathing cycle can be described using the following equation:

$$R_{res} = \frac{60}{T_n^{Ex} + T_n^{In}} (\text{Breaths/min})$$

Respiratory depth (R_{rsd}) denotes the amount of air (tidal volume V_R) that is inhaled or exhaled during a whole breathing cycle. The R_{rsd} values of each respiratory cycle are calculated by the V_R-I equation (The V_R value are tested by pneumatometer, see Fig. S9).

The respiratory pattern of one volunteer was measured in about 210 s with two different respiratory depth (R_{rsd}) and three different respiratory speed (R_{rsp}), including slow (≈12 min^{-1}), medium (≈26 min^{-1}), and rapid (≈60 min^{-1}). The obtained corresponding R_{res} and R_{red} data are shown in Fig. S8-c. For this purpose, a smart wireless mask, which can monitor both exhaled flow humidity and respiratory rate real-timely, is constructed successfully. Furthermore, because of its high sensitivity, the pressure sensor holds great potential to be used for detecting finger (Fig. S10), wrist (Fig. S11) and human voice (Fig. S12) motion activities.

3.1. Real-time high accuracy pulse wave monitoring under body motion interference

Long-term artery pulse waves monitoring in daily life require the sensor to maintain high sensitivity in a large linear detection range, therefore, the sensor can discriminate the subtle change under the interference of strong dynamic pressure caused by body movement. A wearable device consisted of S_4 imbedded in comfortable textiles were assembled for the detection of weak artery pulse waves signal (Fig. 4**b**). To investigate the device's performance under different pressure, we set up three different base pressures (1 kPa, 4 kPa, 10 kPa) on the radial artery (Fig. 4**c-i** and **ii**), which is within the linear detection range of our sensor (< 20 kPa). The pressure is applied accurately by a blood pressure cuff to the sensor (Fig. 4**c-iii** and **iv**), which is among the first linear detection regime of our sensor (< 20 kPa). Fig. 4**d-i** gives the response of the sensor for 10 s, clearly demonstrating that the waveform pattern of the artery pulse can be detected under different applied pressure. Furthermore, from 1 kPa to 10 kPa applied pressure, all the Systolic peak (P_S), point of inflection (P_i), tidal wave (P_T), Valley, and diastolic peaks (P_D) are successfully identified by the sensor output signal. This waveform provides some diagnostic information of cardiovascular disease (such as pulse velocity, time gap and intensity ratio,of peaks) (Fig. 4**d-ii**) [33]. Fig. 4**d-iii** depicts the average current change obtained respective to the artery pulse from the same devices under different applied pressure. It was observed that a much stronger current change (624.7%) was added to the signal when the device was attached with pressure from low (1 kPa) to high (10 kPa). The high sensitivity and large linear detection range of the sensor endow the device to detect a weak pulse signal under large dynamic pressure caused by body movement or ambient variation. As shown in Fig. 4**e**, although the wrist bending caused a large continuous pressure variation (from 1 kPa to 6 kPa), all the weak peak can be identified by the sensor output signal during the whole bending process. In comparison, a gentle touch, a weak wrist bending or even a gentle hand movement would destroy

the signal for narrow response range sensor (Fig. S13), which greatly limits its application in practical use.

To investigate the structural effects of the ISG film on the detection ability of our devices, we compared various PDMS-Gr structure (S_1, S_2, S_4) with different conductivity. The same base pressure (≈4 kPa) is set up to maximize the signal from the wrist pulse. As summarized in Fig. 4**f**, all the typical characteristics of wrist pulses obtained by the above sensors clearly contain P_S, P_i, P_T, Valley, and P_D, suggesting the potential application of these sensors in clinical medicine for pulse measurement. Further quantitative research demonstrated that the S_4 shows a highest peak signal-noise ratio (PSNR) value (78 dB) compared to S_1 (29 dB), S_2 (51 dB) and such commercial pulse sensors as photoplethysmography (PPG) (23 dB) and piezoelectric pulse transducer (PPT) (26 dB) [34,35]. The ultra-high PSNR of S_4 makes the device very sensitive to the weak high frequency waves of pulse signals that contain important clinical messages. As shown in Fig. 4**g**, eight visibility of periodic red line patterns were observed in the short-time Fourier transform frequency spectrum of S_4. In the low frequency range below 5 Hz, four strong periodic lines can be observed, which corresponds to the frequency of pulse velocity (≈0.97 Hz), P_D (≈ 2.14 Hz), P_T (≈ 3.12 Hz) and P_S (≈ 4.10 Hz). Notably, in the high frequency range from 5 Hz up to 10 Hz, four weak yet distinct periodic lines (5.20 Hz, 6.25 Hz, 7.22 Hz, 8.39 Hz) are observed. To the best of our knowledge, these weak signals have not yet been observed and reported due to the limitation of the previously reported wearable sensing technologies. Although we observe periodic lines for S_2 in the high frequency range, the intensities of the lines are lower than those for the S_4 and one weak line in 8.39 Hz almost vanishes. Furthermore, due to the noise interference, few periodic lines can be observed in the frequency spectrum of S_1. Thus, it can be concluded that the enhanced PSNR of the pressure sensor is critical for weak wave detection in pulse signals.

Cardiovascular disease is one of the important causes of death globally. However, it is estimated that 90% of cardiovascular diseases can be prevented by the long-term monitoring of the physiological signal [36,37]. Arterial pulse wave can give important information about the arterial physical situation. Usually, the weak waves in pulse signals are the key element for diagnosing [38]. Our pulse sensor thus provides an excellently noninvasive route to record the weak pulse wave signal. Fig. 5**a** shows the real-time pulse signal when S_4 was placed over the carotid arteries of a 28-year-old man and a 69-year-old man, respectively. The left Figures are the enlarged profiles of one cycle. The comparison of the pressure pulse waves indicates apparent differences between the young and old. To further quantify the difference between the pulse waves, two of the most commonly used parameters are defined: the augmentation index AIx(%) = ± (PS −Pi)/PP= ± ΔP/PP, and the reflection index RI= h/Δt, where h is the subject height, Δt is the time delay between P_S and P_D, while PP is the absolute pulse wave magnitude. As shown in Fig. 5**b**, based on the 10 min continuous arterial pulse waves, a statistical result of the AIx and RI was recorded for the young and old. For the older one, average values of 24.7% and 13.1 m s^{-1} were recorded for the parameters AIx and RI, while for the younger one, values of -21.6% and 8.7 m s^{-1} were recorded. This result is corresponding with early work [39], the distinct difference of AIx and RI between two persons is mainly attributed to the following reasons. Since the young man has better arterial compliance capability, therefore, the pulse wave is spread through the arteries at a lower velocity and the reflected wave also arrives back to the aorta after the late systole, leading to a smaller RI and negative AIx. Furthermore, the frequency spectra of the young and old are significantly different (Fig. 5**c**). On the one hand, for the old one, four strong periodic lines in the low frequency range are higher than the younger subject. On the other hand, at a high frequency range, the periodic line patterns in the frequency spectrums of the old are much weaker than the young. It's worth to point out that more research is needed to study the relationship between the weak peak signal and health state. More valuable information may be discovered through the sensor.

Despite remarkable advances in wearable medical devices, it has not yet been demonstrated with mobile wearable devices which can long-

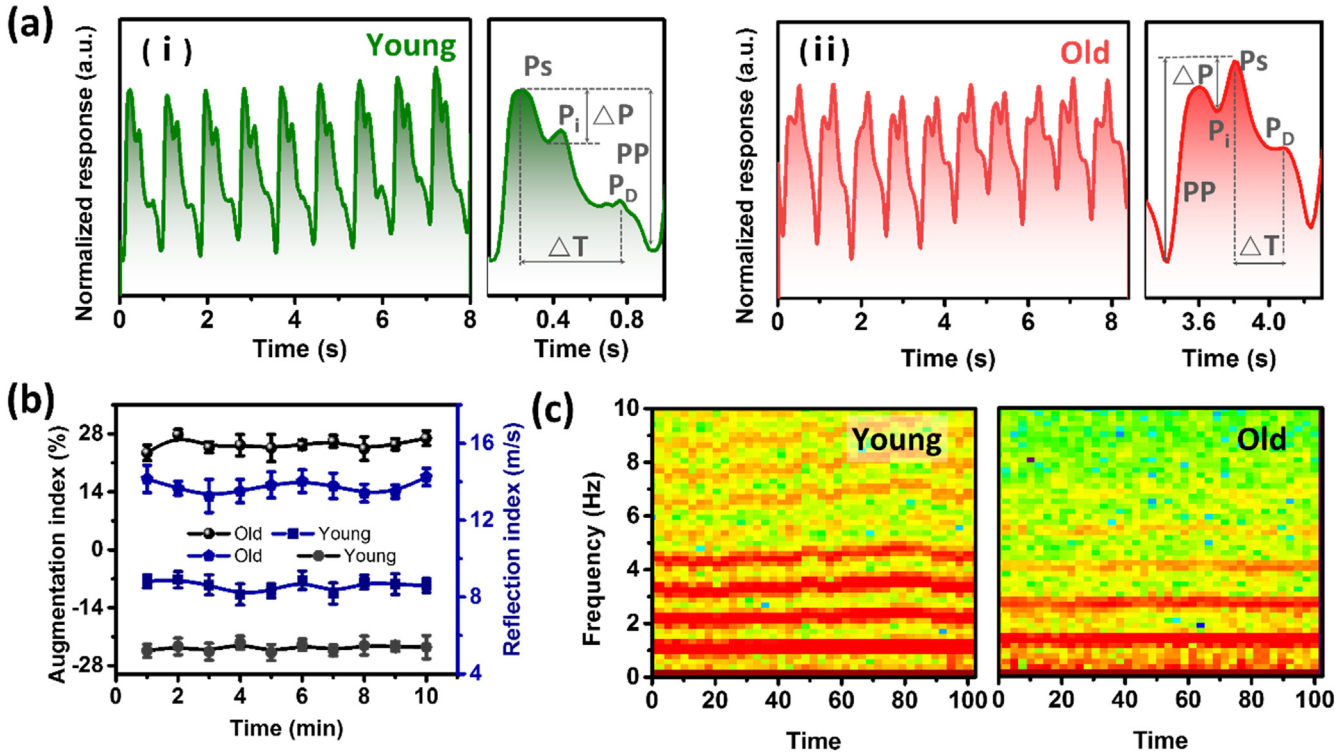

Fig. 5. The sensor for noninvasive arterial physical health situation monitoring. (a) The real-time carotid arteries pulse signal of a 28-year-old man (i) and a 69-year-old man (ii). c) Comparison of the RI value and AIx value between the young and the old. (c) The detected frequency spectrum of young volunteer and old volunteer using the S_4 under same applied pressure.

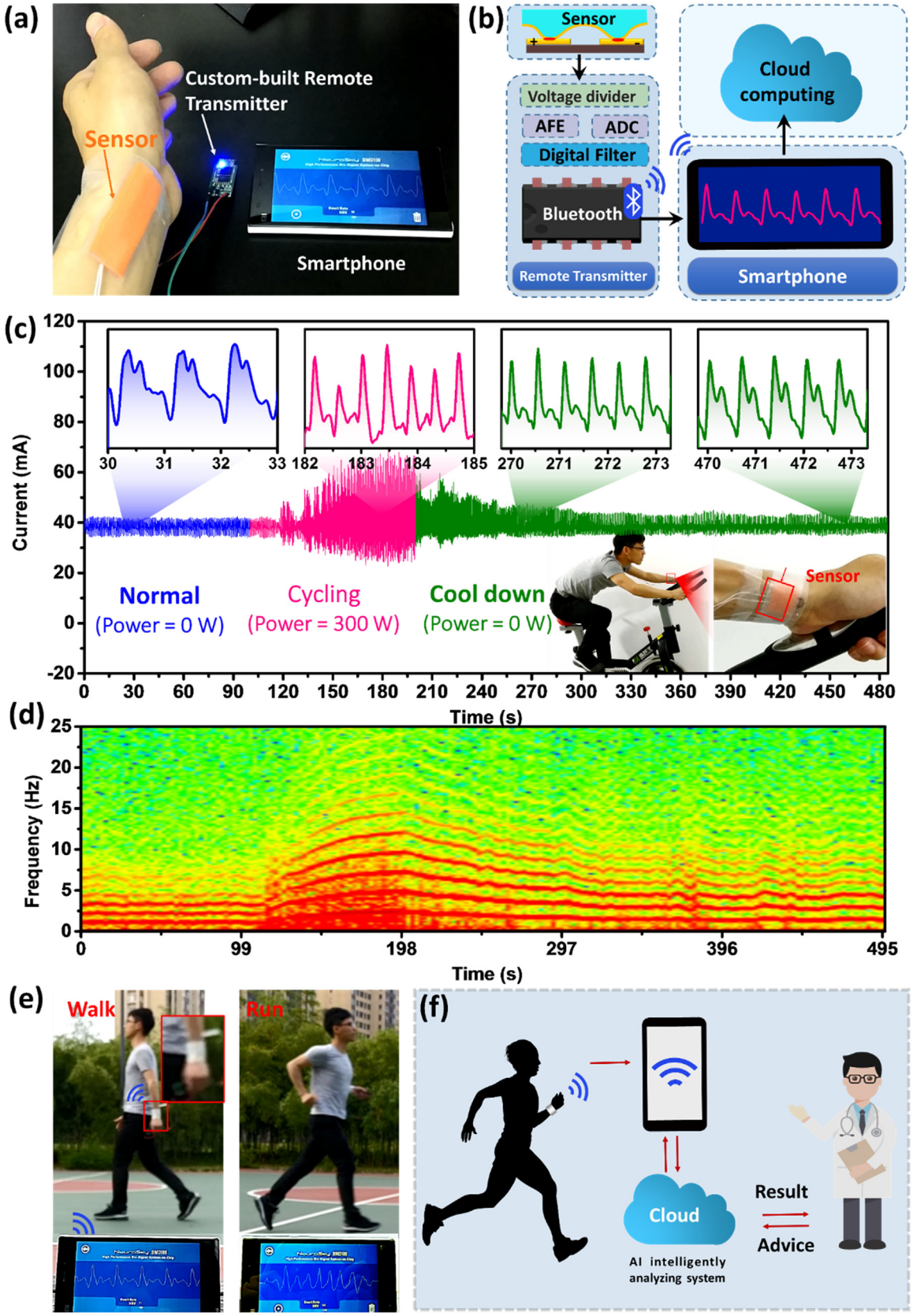

Fig. 6. Design and application high accuracy wireless wearable pulse monitoring system. (a) Photo of the wearable device on an arterial pulse real-time monitoring subject. (b) Schematic illustrations of the wearable human arterial pulse monitoring device system. (c) The real-time artery pulse signal of and the extracted interpreted waveforms (without smooth) measured by a pressure S_4 mounted onto the radial artery of the wrist during cycling. (d) The frequency spectrum of the corresponding output of the pulse signal during cycling. (e) Image of wireless health monitoring system applied during the process of walking and running. (f) Illustration of intelligent mobile diagnosis system based on our sensor.

termly monitor such weak signal during daily activities or fitness due to their sensitivity and vulnerability to body movement. In this study, the S_4 device presents a robust piezo-resistive pressure detection device with a wide linear relationship, which enables the device to discriminate a subtle change at the relatively high-pressure regime. Therefore, the device could obtain accurate information from the sensor output even under the strong interference of body movement. Herein, we designed a real-time artery plus monitoring prototype, which is capable of detecting the weak plus signal under dynamical situation (Fig. 6**a** and **b**). Fig. 6**c** represents the real-time current response of the pressure sensor mounted onto the radial artery of the wrist during cycling process, in which various complex physical forces including the pulse waveforms, breath, muscular and body movement. The applied pressure was caused by the sensor being affixed by a comfortable medical tape on the wrist, to be ≈ 4 kPa to maximize the signal from the wrist pulse. It was observed that the pulse waveforms dominantly visualized even under complex physical forces interference. To precisely extract the pulse signal waveforms from the retrieved data and exclude the low-frequency interference signal from random body movement, fast Fourier transform (FFT) with a bandpass filter from 0.1 to 25.0 Hz was used to filter the as-measured waveforms (Fig. S14). Comparing to commercialized pulse monitoring wearable device based on PPG, our pressure sensors could detect the subtle difference in the pulsations of different physiological state under dynamic interference of body movement real-timely (**Video-2**). The inserted Figure in Fig. 6**c** clearly shows the continuous variation of pulse waveforms, such as shape, intensity (normalized statistical data are shown in Fig. S15). Furthermore, as shown in Fig. 6**d**, the frequency spectra of the waveforms not only show the real-time pulse velocity information during cycling but also can accurately identify the continuous variation information of the weak feature peak. Based on these results, this device holds great potential to be used in intelligent mobile diagnosis system, which can continuously acquire pulse wave information during daily life and fitness. As shown in Fig. 6**e**, the wearable device can easily detect pulse signal during human activity, such as walking or even running (**Video-3**). Through this intelligent terminal and combining with the general film and artificial intelligence (AI) technology, we can get expert advice and other feedback for a patient (Fig. 6**f**). The system holds great potential to be used in on-line monitoring, intelligent mobile diagnosis, and even cardiovascular disease prevention.

Supplementary material related to this article can be found online at doi:10.1016/j.nanoen.2019.02.036.

4. Conclusion

In conclusion, through theoretical model analysis, this work has provided a new perspective to balance the trade-off between sensitivity and linearity of pressure sensor through regulating the conductivity and thickness of sensing layer, in addition to designed new micro/nanostructure morphologies. Furthermore, we developed an alternative strategy to produce high conducting graphene thin film, which could be then transferred and self-attach to micro-patterned elastomer for the fabrication of sensor devices. As a result, the piezo-resistive pressure sensor device can perform unprecedented high yet tunable sensitivity (1.04–1875.5 kPa^{-1}) in a large linear detection range (1–40 kPa). These promising advantages of our sensor enable the recording of the very weak and subtle arterial pulse signal information under applied pressures, thus enabling the measurement of accurate information arterial pulse. Furthermore, a universal high accuracy wireless and wearable pulse monitoring system was built and first used to monitor real-time arterial pulse signal during excise. In view of the facile and scalable preparation of our sensory materials as well as their robust sensing ability, the proposed strategy holds great potential to be constructed as practically useful physiological real-time monitoring devices.

Acknowledgment

This work was supported by the National Natural Science Foundation of China (51573203, 5150321651622205, 61675027, 51432005, 61505010 and 51502018), the Bureau of International Cooperation of Chinese Academy of Sciences (174433KYSB20170061), Key Research Program of Frontier Science, Chinese Academy of Sciences (QYZDB-SSW-SLH036), National Key R & D Project from Minister of Science and Technology, China (2016YFA0202703), Beijing City Committee of Science and Technology (Z171100002017019 and Z181100004418004), and Beijing Natural Science Foundation (4181004, 4182080, 4184110, 2184131 and Z180011).

Author contributions

J.H., W.L., C.F.P., and T.C. conceived and designed the experiments. J.H., L.Z., J.W.S, Y.L. performed the experiments. P.X. and J.W.S contributed to materials. J.H., L.Z., J.W.S, S.W.K., and Y.L. contributed to characterization, analysis, and discussion. J.H., W.L., C.F.P., S.W.K., and T.C. co-wrote the paper.

Notes

The authors declare no competing financial interest.

Appendix A. Supporting information

Supplementary data associated with this article can be found in the online version. Photograph of transferred ISG film with different layers on a glass substrate. Photograph and SEM images of macro-pattered PDMS-Gr elastomer. Photograph and SEM images of ISG film. The displacement distribution of the simulation results for the macro-pattered elastomer at different external loading pressure. Real-time I-t curves of the pressure sensor for 15,000 loading/unloading cycles. Response and recovery time of the pressure sensor. Sensor application in human respiratory monitoring. Fitted breath air volume as a function of current. Real-time monitoring of finger and wrist gestures. The application of the pressure sensor for throat phonation. The pulse signal of the narrow response range pressure sensor. The real-time pulse wave signal of S_4 under body movement interference. The statistical data of normalized heartbeat intensity.

Appendix A. Supporting information

Supplementary data associated with this article can be found in the online version at doi:10.1016/j.nanoen.2019.02.036.

References

[1] Y. Khan, A.E. Ostfeld, C.M. Lochner, A. Pierre, A.C. Arias, Adv. Mater. 28 (2016) 4373–4395.
[2] Y.S. Rim, S.-H. Bae, H. Chen, N. De Marco, Y. Yang, Adv. Mater. 28 (2016) 4415–4440.
[3] X. Wang, L. Dong, H. Zhang, R. Yu, C. Pan, Z.L. Wang, Adv. Sci. 2 (2015) 1500169.
[4] A. Chortos, J. Liu, Z. Bao, Nat. Mater. 15 (2016) 937–950.
[5] Z.L. Wang, J. Chen, L. Lin, Energ. Environ. Sci. 8 (2015) 2250–2282.
[6] C. Pang, J.H. Koo, A. Nguyen, J.M. Caves, M.-G. Kim, A. Chortos, K. Kim, P.J. Wang, J.B.H. Tok, Z. Bao, Adv. Mater. 27 (2015) 634–640.
[7] X. Wang, Z. Liu, T. Zhang, Small 13 (2017) 1602790.
[8] Y. Liang, P. Xiao, S. Wang, J. Shi, J. He, J. Zhang, Y. Huang, T. Chen, J. Mater. Chem. C 6 (2018) 6666–6671.
[9] S. Wang, P. Xiao, Y. Liang, J. Zhang, Y. Huang, S. Wu, S.-W. Kuo, T. Chen, J. Mater. Chem. C 6 (2018) 5140–5147.
[10] J. He, P. Xiao, J. Shi, Y. Liang, W. Lu, Y. Chen, W. Wang, P. Théato, S.-W. Kuo, T. Chen, Chem. Mater. 30 (2018) 4343–4354.
[11] G.Y. Bae, S.W. Pak, D. Kim, G. Lee, D.H. Kim, Y. Chung, K. Cho, Adv. Mater. 28 (2016) 5300–5306.
[12] X. Wang, Y. Gu, Z. Xiong, Z. Cui, T. Zhang, Adv. Mater. 26 (2014) 1336–1342.
[13] Z. Zhao, C. Yan, Z. Liu, X. Fu, L.-M. Peng, Y. Hu, Z. Zheng, Adv. Mater. 28 (2016) 10267–10274.
[14] Y. Zang, F. Zhang, C.-A. Di, D. Zhu, Mater. Horiz. 2 (2015) 140–156.

[15] S.C.B. Mannsfeld, B.C.K. Tee, R.M. Stoltenberg, C.V.H.H. Chen, S. Barman, B.V.O. Muir, A.N. Sokolov, C. Reese, Z. Bao, Nat. Mater. 9 (2010) 859–864.
[16] B.C.K. Tee, A. Chortos, R.R. Dunn, G. Schwartz, E. Eason, Z. Bao, Adv. Funct. Mater. 24 (2014) 5427–5434.
[17] K.Y. Lee, H.-J. Yoon, T. Jiang, X. Wen, W. Seung, S.-W. Kim, Z.L. Wang, Adv. Energy Mater. 6 (2016) 1502566.
[18] Y. Pang, K. Zhang, Z. Yang, S. Jiang, Z. Ju, Y. Li, X. Wang, D. Wang, M. Jian, Y. Zhang, R. Liang, H. Tian, Y. Yang, T.-L. Ren, ACS Nano 12 (2018) 2346–2354.
[19] A.K. Geim, Science 324 (2009) 1530–1534.
[20] K.S. Novoselov, V.I. Fal'ko, L. Colombo, P.R. Gellert, M.G. Schwab, K. Kim, Nature 490 (2012) 192–200.
[21] P. Xiao, C. Wan, J. Gu, Z. Liu, Y. Men, Y. Huang, J. Zhang, L. Zhu, T. Chen, Adv. Funct. Mater. 25 (2015) 2428–2435.
[22] L. Dong, J. Yang, M. Chhowalla, K.P. Loh, Chem. Soc. Rev. 46 (2017) 7306–7316.
[23] K.P. Loh, Q. Bao, P.K. Ang, J. Yang, J. Mater. Chem. 20 (2010) 2277–2289.
[24] X. Li, G. Zhang, X. Bai, X. Sun, X. Wang, E. Wang, H. Dai, Nat. Nanotechnol. 3 (2008) 538.
[25] T. Zhang, Z. Liao, L.M. Sandonas, A. Dianat, X. Liu, P. Xiao, I. Amin, R. Gutierrez, T. Chen, E. Zschech, G. Cuniberti, R. Jordan, Nat. Commun. 9 (2018) 4051.
[26] L. Niu, J.N. Coleman, H. Zhang, H. Shin, M. Chhowalla, Z. Zheng, Small 12 (2016) 272–293.
[27] P. Xiao, J. Gu, J. Chen, J. Zhang, R. Xing, Y. Han, J. Fu, W. Wang, T. Chen, Chem. Commun. 50 (2014) 7103–7106.
[28] P. Xiao, J. Gu, C. Wan, S. Wang, J. He, J. Zhang, Y. Huang, S.-W. Kuo, T. Chen, Chem. Mater. 28 (2016) 7125–7133.
[29] J. Chun, K.Y. Lee, C.Y. Kang, M.W. Kim, S.W. Kim, J.M. Baik, Adv. Funct. Mater. 24 (2014) 2038–2043.
[30] C.-L. Choong, M.-B. Shim, B.-S. Lee, S. Jeon, D.-S. Ko, T.-H. Kang, J. Bae, S.H. Lee, K.-E. Byun, J. Im, Y.J. Jeong, C.E. Park, J.-J. Park, U.I. Chung, Adv. Mater. 26 (2014) 3451–3458.
[31] N. Luo, Y. Huang, J. Liu, S.-C. Chen, C.P. Wong, N. Zhao, Adv. Mater. 29 (2017) 1702675.
[32] H. Jin, Y.S. Abu-Raya, H. Haick, Adv. Healthc. Mater. 6 (2017) 1700024.
[33] M.F. O'Rourke, Am. Heart J. 82 (1971) 687–702.
[34] S. Dash, K.H. Shelley, D.G. Silverman, K.H. Chon, IEEE Trans. Bio-Med. Eng. 57 (2010) 1099–1107.
[35] T. Yamakoshi, J. Lee, K. Matsumura, Y. Yamakoshi, P. Rolfe, D. Kiyohara, K.-I. Yamakoshi, PLoS One 10 (2015) e0143506.
[36] H.C. McGill Jr, C.A. McMahan, S.S. Gidding, Circulation 117 (2008) 1216–1227.
[37] H. Ouyang, J. Tian, G. Sun, Y. Zou, Z. Liu, H. Li, L. Zhao, B. Shi, Y. Fan, Y. Fan, Z.L. Wang, Z. Li, Adv. Mater. 29 (2017) 1703456.
[38] K. Kohara, Y. Tabara, A. Oshiumi, Y. Miyawaki, T. Kobayashi, T. Miki, Am. J. Hypertens. 18 (2005) 11S–14S.
[39] W.W. Nichols, Am. J. Hypertens. 18 (2005) 3S–10S.

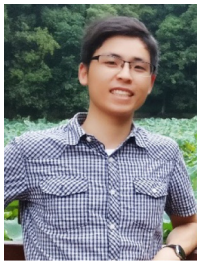

Jiang He received his MS degree from Ningbo University, China in 2016. Currently, he is a Ph.D. student in the Ningbo Institute of Materials Technology and Engineering, Chinese Academy of Sciences, under the supervision of Prof. Tao Chen. His research interests focus on the smart polymers and carbon nano materials hybrid with applications as actuators and sensors.

Dr. Peng Xiao received his Ph.D. degree in polymer chemistry and physics from Ningbo Institute of Materials Technology and Engineering, Chinese Academy of Sciences, under the supervision of Prof. Tao Chen. Now he joint Tao Chen's group as a postdoctoral research fellow. His current research is focused on the macroscopically, self-assembly of 1D and 2D of carbon-based materials into 2D ultrathin films at air/water interface to explore their potential applications in actuators, sensors.

Prof. Wei Lu was born in Bengbu, China in 1987 and received his Ph.D. degree in polymer chemistry and physics from Zhejiang University in China (2014). Soon afterwards he joined Ningbo Institute of Materials Technology and Engineering, Chinese Academy of Science as a postdoctoral research fellow. He was promoted to associate professor in December 2016. His current research is focused on the fabrication of stimuli-responsive functional materials including hydrogels and photoluminescent polymers and their applications in shape memory and chemical sensing.

Jiangwei Shi received his M.S. degree in Materials Engineering from University of Science and Technology of China (USTC) in 2018 under the guidance of Prof. Lei Shi from USTC and Prof. Tao Chen from Ningbo Institute of Materials Technology and Engineering, Chinese Academy of Sciences. His main research interests and activities are polymer composites based on carbon-films as sensors.

Ling Zhang received her bachelor degree of polymer science and engineering from Southwest Jiaotong University, China in 2017. Currently, she is a master candidate in the Ningbo Institute of Materials Technology and Engineering, Chinese Academy of Sciences, under the supervision of Prof. Tao Chen. Her research interests focus on the smart polymers and carbon nano materials hybrid with applications as actuators and sensors.

Yun Liang received his bachelor's degree from Southwest University of Science and Technology. Currently, He is a Ph.D. student in the Ningbo Institute of Materials Technology and Engineering, Chinese Academy of Sciences, under the supervision Professor Tao Chen and Youju Huang. His current research interests focus on polymer/Carbon-based 2D hybrid materials and their applications as sensors and actuators.

Prof. Caofeng Pan received his B.S. degree (2005) and his Ph.D. (2010) in Materials Science and Engineering from Tsinghua University, China. He then joined the Georgia Institute of Technology as a postdoctoral fellow. He is currently a professor and a group leader at Beijing Institute of Nanoenergy and Nanosystems, Chinese Academy of Sciences since 2013. His main research interests focus on the fields of piezotronics/piezo-phototronics for fabricating new electronic and optoelectronic devices, and self-powered nanosystems. Details can be found at http://www.piezotronics.cn.

Prof. Tao Chen received his Ph.D. in polymer chemistry and physics from Zhejiang University in 2006. After his postdoctoral training at the University of Warwick (UK), he joined Duke University (USA) as a research scientist. He then moved back to Europe as an Alexander von Humboldt Research Fellow at Technische Universität Dresden, Germany. Since 2012, he is a full-time professor at Ningbo Institute of Materials Technology and Engineering, Chinese Academy of Sciences. His research interests include smart polymers and their hybrid systems with applications as actuators, shape memory polymers, and chemical sensing.